

Supporting information of

Effect of Stiffness on the Dynamics of Entangled Nanofiber Networks at Low Concentration

Ahmad Reza Motezakker^{,†,‡}, Andrés Córdoba[¥], Tomas Rosén^{‡,¶}, Fredrik Lundell[†], L. Daniel Söderberg^{*,‡,¶}*

Affiliations:

[†]Department of Engineering Mechanics, KTH Royal Institute of Technology; Stockholm, SE-10044, Sweden

[‡]Wallenberg Wood Science Center, KTH Royal Institute of Technology; Stockholm, SE-10044, Sweden

[¥]Pritzker School of Molecular Engineering, University of Chicago; Chicago, Illinois, 60637, USA

[¶]Fiber and Polymer Technology Department, KTH Royal Institute of Technology; Stockholm, SE-100 44, Sweden

S1. Simulation methods

Coarse-graining simulations. Polymers and the fluid (liquid solvent) are the two basic elements of such systems that must be accounted for in the modeling procedure. The ESPResSo software package was used for all simulations. A bead-spring chain model was used to represent the polymer, with a Weeks-Chandler-Andersen (WCA) potential set up between the beads as below

$$U_{WCA}(r) = \begin{cases} 4\epsilon \left[\left(\frac{\sigma}{r} \right)^{12} - \left(\frac{\sigma}{r} \right)^6 \right] + \epsilon, & \text{if } r < 2^{\frac{1}{6}} \sigma, \\ 0, & \text{else,} \end{cases}$$

where σ is the diameter of the beads and ϵ represents the energetic pre-factor with Boltzmann constant k_B and temperature T . An attractive potential is used to explicitly resolve each polymer chain utilizing MD beads that are coupled to one another; in this case, we use a standard harmonic interaction in the form of

$$\varphi_{harm} = \frac{1}{2} k (r - r_0)^2,$$

where r is the distance between two adjacent MD beads in a polymer chain, r_0 is the equilibrium distance of the potential, and k is the spring constant that defines the bond stiffness. The angle potential is used to directly tune the nanofiber bending rigidity as follows.

$$V(\phi) = K \left(1 - \cos(\phi - \phi_0) \right),$$

where K is the bending constant and ϕ_0 is the equilibrium bond angle in radians ranging from 0 to π .

We coupled the beads to a thermalized lattice-Boltzmann (LB) fluid to include hydrodynamic interactions. We were able to successfully couple the LB fluid and the MD beads relying on the point-coupling strategy provided in ¹, which coupling force is as follows

$$\vec{F} = -\gamma (\vec{u}_{fluid} - \vec{u}_{bead}),$$

where γ is the friction parameter, \vec{u}_{fluid} is the fluid velocity, and \vec{u}_{bead} is the velocity of the bead.

Therefore, the equation of motion is the same as the Langevin equation, except that it considers the bead's relative velocity to the fluid as follows.

$$m_i \dot{v}_i(t) = f_i - \gamma(v_i(t) - u(x_i(t), t)) + \sqrt{2\gamma k_B T} \eta_i(t)$$

Here, f_i represents all deterministic forces resulting from interactions and η a random thermal force.

The friction term allows for dissipation in the surrounding fluid, whereas the random force simulates collisions of the particle with solvent molecules at temperature T and meets the condition

$$\langle \eta(t) \rangle = 0, \text{ and } \langle \eta_i^\alpha(t) \eta_j^\beta(t') \rangle = \delta_{\alpha\beta} \delta_{ij} \delta(t - t'),$$

where $\langle . \rangle$ denotes the ensemble average, α, β are spatial coordinates, and δ is the Kronecker delta.

The LB fluid is discretized using a D3Q19 geometry with a grid spacing of $a = \sigma$.

ESPResSo employs the notion of simulation units, which enables the user to freely choose the system's mass, length, and energy scales, which together define all other parameters. For additional details on parameter selection, choice of observables, and other relevant information, please refer to the Supporting Information.

Micro-rheology analysis. In the technique called passive microrheology the mean-squared displacement (MSD) of a micron-sized bead embedded in a viscoelastic fluid is used to infer the dynamic modulus, $G^*(\omega)$, of the fluid. To obtain the MSD of the probe bead, the γ -positions ($\gamma = (x, y, z)$) of the probe bead as a function of time, $r_{b,\gamma}(t)$, is tracked. Where $t = i \Delta t$, $1/\Delta t$ is the sampling frequency of the measurement device, N is the total number of measurements and $i = 0, 1, 2, 3, \dots, N$. The first step in the data analysis requires the calculation of the mean-squared displacement (MSD) of the probe bead,

$$\langle \Delta r^2(\tau) \rangle := \frac{1}{n} \sum_{\gamma} \sum_{i=1}^n \Delta r_{i,\gamma}^2(\tau)$$

where

$$\Delta r_{i,\gamma}^2(\tau) := [r_{b,\gamma}(t+\tau) - r_{b,\gamma}(t)]^2, n = N - \tau/\Delta t, \tau$$

is the lag time and the sub-index $\gamma = \{x, y, z\}$ indicates the spatial direction of the measurement.

In order to obtain an estimate of the statistical uncertainty in $G^*(\omega)$ obtained from passive microrheology, one needs to start by estimating the statistical error in the MSD. A common omission in the analysis of passive microrheology data is to neglect correlations inherent in the bead position data. These correlations are very important in viscoelastic materials. In a typical viscoelastic fluid, the uncertainty in the MSD of the probe bead can be as high as 20%. The highest errors occur at long lag times. At those long times, the uncertainty is underestimated by a factor of about 20 if the correlation in the bead position data is neglected². Here we use the Microrheology Uncertainty Calculation Helper (MUnCH)^{2,3} to calculate $\langle \Delta r^2(\tau) \rangle$ and its uncertainty, $\sigma(\langle \Delta r^2(\tau) \rangle)$. By using repeated block transformations, MUnCH can correctly estimate the statistical error of any autocorrelation at any given lag time. Examples of MSDs of the probe bead and their uncertainties in a cellulose solution with different mesh sizes, ξ_p/L , are shown in Fig. S7. Note that the overall magnitude of the MSD of the probe bead decreases with decreasing mesh size of the cellulose solution.

In passive microrheology, the dynamic modulus of the host medium, $G^*(\omega)$, is calculated using the Generalized Stokes-Einstein Relation (GSER). However, applying the original GSER to molecular dynamics simulations with periodic boundary conditions can result in overestimated $G^*(\omega)$ values because of the hydrodynamic interaction between the probe bead and its periodic images. A correction to the GSER has been derived by implementing an analytical solution for Stokes drag on a periodic array of spheres, which allows smaller box sizes to be simulated while still retaining accuracy⁴. This relation has been called the hydrodynamic Generalized Stokes-Einstein Relation (HGSEr). The HGSEr allows the use of smaller box sizes, reducing computational costs by more than an order of magnitude⁴

$$G^*(\omega) = \left(K_S \frac{f_V}{f_M} \right)^{-1} \left(\frac{k_B T}{\pi R i \omega \langle \Delta r^2[\omega] \rangle} \right)$$

Where R is the bead radius, k_B is the Boltzmann constant, T is the temperature, ω is the radial frequency and

$$\langle \overline{\Delta r^2}[\omega] \rangle := \int_0^\infty \langle \Delta r^2(\tau) \rangle e^{-i\omega\tau} d\tau$$

is the one-sided Fourier transform of the MSD of the probe bead.

The factor

$$\left(K_S \frac{f_V}{f_M} \right)^{-1}$$

accounts for the interactions of the probe bead with its periodic images, where f_M is the mass fraction and f_V the volume fraction of fluid (solvent + cellulose fibers) in the simulation box. For the systems considered in this work $f_M \approx 0.5$ and $f_V \approx 0.95$, the exact values for each particular system are calculated and used in the data analysis of each system. The function K_S as a function of the volume fraction of spheres $\phi = 4\pi/3 \left(R/L_{box} \right)^3$ is given by ⁴

$$K_S^{-1} = 1 - 1.7601\phi^{1/3} + \phi - 1.5593\phi^2 + 3.9799\phi^{8/3} - 3.0734\phi^{10/3}$$

Where R is the radius of the probe bead and L_{box} is in the systems considered here $R = 166.66 \sigma$,

$T = 300 K$ and $L_{box} = 600 \sigma$ is the length of the cubic periodic box.

To calculate $\langle \overline{\Delta r^2}[\omega] \rangle$ we use a method that does not require fitting $\langle \Delta r^2(\tau) \rangle$ with an analytic function to perform the one-sided Fourier transform ⁵. Specifically, we use

$$i\omega \langle \overline{\Delta r^2}[\omega] \rangle \approx (2\pi i)^{-\alpha(\omega)} \langle \Delta r^2(2\pi/\omega) \rangle \Gamma[1 + \alpha(\omega)],$$

where

$$\alpha(\omega) := \frac{d \log \Delta r^2(\tau)}{d \log \tau} \bigg|_{\tau=2\pi/\omega}$$

is the local power law exponent of $\langle \Delta r^2(\tau) \rangle$ and $\Gamma(\dots)$ is the Euler gamma function. The values of $\alpha(\omega)$ for the MSDs shown in Fig. S7B. In general, α varies between diffusive, $\alpha \approx 1$, and sub-diffusive $\alpha \approx 0.3$ in the range of lag times sampled here. At long times the scaling exponents are diffusive, *i.e.* $\alpha \approx 1$, and reflect the diffusion of the probe bead in the solvent. The minimum in α moves to shorter times (*i.e.* higher frequencies) and becomes deeper as the mesh size of the solution, ξ/L , is made smaller. The uncertainty in $\langle \overline{\Delta r^2}[\omega] \rangle$ is estimated by standard propagation of error as

$$\delta \langle \overline{\Delta r^2}[\omega] \rangle = \sqrt{\left[\frac{d \langle \overline{\Delta r^2}[\omega] \rangle}{d \langle \Delta r^2(\tau) \rangle} \sigma(\langle \Delta r^2(\tau) \rangle) \right]^2 + \left[\frac{d \langle \overline{\Delta r^2}[\omega] \rangle}{d\alpha} \delta\alpha \right]^2},$$

whereas pointed out before $\sigma(\langle \Delta r^2(\tau) \rangle)$ is obtained using MUnCH² and the uncertainty in α is obtained from propagation of error,

$$\delta\alpha = \sqrt{\left[\frac{d\alpha}{d \langle \Delta r^2(\tau) \rangle} \sigma(\langle \Delta r^2(\tau) \rangle) \right]^2}.$$

Using the above equation, the uncertainty in $G^*(\omega)$ is obtained by the propagation of error as,

$$\delta G^*(\omega) = \sqrt{\left[\frac{dG^*(\omega)}{d \langle \overline{\Delta r^2}[\omega] \rangle} \delta \langle \overline{\Delta r^2}[\omega] \rangle \right]^2}.$$

The storage modulus, $G'(\omega) = \text{Re}\{G^*(\omega)\}$ and its uncertainty, the loss modulus,

$G''(\omega) = \text{Im}\{G^*(\omega)\}$, and its uncertainty are shown in the main text. The zero-shear viscosity is obtained from

$$\eta = \int_0^\infty G(t) dt,$$

where the relaxation modulus, $G(t)$, is related to dynamic modulus by

$$G^*(\omega) = i\omega \overline{\mathcal{F}}[G(t)] = i\omega \int_0^\infty G(t) e^{-i\omega t} dt.$$

S2. Simulation parameters

ESPResSo employs the notion of simulation units, which enables the user to freely choose the system's mass, length, and energy scales, which together define all other parameters. The nanofiber width, which we assumed to be 3 nm, is the shortest length scale in the system; hence, we define length scale $[x]=3$ nm. As simulations are conducted at $T = 25^\circ \text{C}$, we employ $T \approx 300 \text{ K}$ in our model and provide the energy scale $[E]=k_B \cdot 300 \text{ K}$. The unit mass of a single bead was set to $[m]=1$.

In implicit-solvent simulations, it is not possible to simply calculate the time scale by translating mass, energy, and length units to time units in a simulation as

$$[t]=[x] \cdot \sqrt{\frac{[m]}{[E]}},$$

because the implicit solvent (LB fluid) determines the viscosity of the solvent, which does not enter the time unit calculation. Therefore, we determine the time unit by using the rotational diffusion coefficient of a stiff rod of the same length as the shortest nanofiber in our system. According to Doi's prediction for a rigid rod

$$D_r \approx \frac{3 k_B T \left(2 \ln \left(\frac{2L}{b} \right) - 1 \right)}{16 \pi \mu \left(\frac{L}{2} \right)^3},$$

where L is the rod length, b is the width, and μ is the dynamic viscosity of the solvent, which is water in our case $\mu_w \approx 8.9 \times 10^{-4} \text{ Pa.s}$. D_r^{-1} has the unit of time, and our simulations are on the order of $[t] \approx 50 \text{ ns}$. An outline of the simulation unit system's parameters for a few representative system parameters is presented in Table. S1.

S3. System setup

First, a cubic periodic box is defined for the simulations. To avoid any boundary effect on the nanofibers' dynamics, we ensure that the box size exceeds the nanofiber length. for the presented simulations, we have kept the minimum size of $1.3 L$ for the box size, where L is the nanofiber length. The following step is to define polymer chains using the so-called bead spring model. In order to mimic high-charged tempo cellulose nanofiber (CNF), we choose nanofiber lengths that are within the reported length distribution of this particular CNF type ($50 < AR < 300$). Assuming that the cross section of the fibers is circular, the area moment of inertia can be determined as $I = \pi \sigma^4 / 64$, and area as $A = \pi \sigma^2 / 4$. The bead-spring model is able to separate the Young's modulus and the bending rigidity of the coarse-grained polymer since they are driven by bond and angle terms, respectively. The bond potential is given by

$$\varphi_{harm} = \frac{k}{2} (r - r_0)^2,$$

and the semiflexible nanofiber has a modulus proportional to its spring constant given by $k = AE / r_0$, where E is Young's modulus and A is the cross-sectional area of the nanofiber. To have direct control over the bending rigidity, the angle potential is chosen accordingly. A polymer chain's bending energy is given by

$$\begin{aligned} E_B &= \frac{\kappa}{2} \int_0^l C^2 ds = \frac{\kappa}{2} \int_0^l \left| \frac{\delta T}{\delta s} \right|^2 ds = \frac{\kappa}{2} r_0 \sum_i \left(\frac{\Delta T}{r_0} \right)^2 \\ &= \frac{\kappa}{r_0} \sum_i (1 - \cos(\pi - \theta)), \quad 0 < \theta < \pi \end{aligned}$$

where κ is bending rigidity, C is local curvature, l is the contour length, and T is unit tangent vector.

Here the angel potential is chosen as $V_{bending}(\theta) = \kappa / r_0 (1 - \cos(\pi - \theta))$ and the relationship between Young's modulus and bending rigidity may be expressed as $\kappa = EI / r_0$. It is possible to test this assumption by juxtaposing the computed bending rigidity of coarse-grained semiflexible polymer chains from simulations with the bending rigidity specified in the angle potential. I brief, the bending rigidity of a coarse-grained semiflexible polymer chain may be determined by clamping one end and monitoring the thermally-induced variation of the other end as

$$\kappa^* = \frac{k_B T L^3}{3 \langle \delta u(L)^2 \rangle}$$

where L is the length of the semi-flexible polymer chain and $\delta u(L) = u(L) - \langle u(L) \rangle$ is the deviation of the free end from its average position⁶. Although there is a natural high variance in measured bending rigidity by applying thermally generated contour fluctuations, the assigned bending rigidity and the observed bending rigidity are in agreement with an acceptable error (see Fig S.1).

This allows us to readily determine the nanofibers' persistence length $L_p = \kappa/k_B T$. Finally, we model the CNFs using the Young's modulus given in the literature, which is in the range of 4.5–18.4 GPa for CNF⁷.

When the nanofibers are built, we scatter them randomly within the box. Thus, it is conceivable for particles to overlap, resulting in a very strong force of repulsion. In this scenario, numerical instability prevents us from integrating the equation of motion. To remove the overlapping, we place constraints on the maximum force that may act between two particles, integrate the equation of motion, and gradually increase the force limit between two particles. Next, we let the chains stabilize by integrating the equation of motion for a while. In the next step, we couple the beads to the fluid by defining the LB fluid and its associated parameters and then applying the LB thermostat to define the friction coefficient. Here, we integrate the equation of motion to warm up the system, including the nanofibers and the LB fluid. The size of the system, such as the number of particles and the length of the polymer, greatly affects the number of steps for the warm-up operation. At long last, we've reached the stage where we can begin integrating the system that records trajectories and other observables. A demonstration of nanofiber modeling for the special situation of $L_p/L = 1.5$ and $\xi_p/L = 0.12$ in Fig. S2. In supplementary movie S1, the dynamics of nanofiber simulations are also shown for the same case.

S4. Observables

Since the position and velocity of each bead are sampled in each time step of the simulations, practically all the system's statistics are accessible. When reporting observables, data must be

averaged throughout all chains and measurements taken at different times. This is achieved via the use of ensemble averaging, $\langle \cdot \rangle$.

Each nanofiber chain is composed of N beads with an end-to-end vector connecting the first bead to the final bead as $\mathbf{R}(t) = \mathbf{r}_N(t) - \mathbf{r}_1(t)$. For internal bending relaxation analysis, end-to-end vector fluctuations are used as

$$\delta R^2(\tau) = \langle (|\mathbf{R}(t+\tau)| - |\mathbf{R}(t)|)^2 \rangle$$

Since the arc length of a polymer remains constant as it fluctuates, the size of the end-to-end vector must be smaller than the actual length of the polymer itself. These fluctuations enable the polymer to reptate along its baseline axis in a semi-dilute environment, when the polymer concentration is high enough that the entanglement length (L_e) becomes less than the persistence length (L_p). It should be noted, nonetheless, that nanofiber rotation plays no role in $\delta R^2(t)$.

Granek⁸ showed that at short times $\delta R^2(t)$ is roughly

$$\delta R^2(t) \simeq \text{const } L \left(\frac{k_B T}{\kappa} \right)^{5/4} \left(\frac{k_B T}{\mu} t \right)^{3/4}$$

And on the other hand, as $t \rightarrow \infty$ end-to-end fluctuations saturate to

$$\delta R^2 = \frac{1}{45} \left(\frac{k_B T}{\kappa} \right)^2 L^4$$

What this implies is that δR^2 acts like $t^{3/4}$ for short times until internal relaxation time, but eventually saturates to $L^4/45L_p^2$.

It is generally expected that the nanofibers' contour would bend less dramatically in semi-flexible circumstances, where $L_p \gg L$, than in flexible ones, where $L_p \ll L$. Therefore, we examine the orientation of the end-to-end vector to assess the rotational motion of the nanofibers. We calculate mean squared angular displacement (MSAD) for the unit vector of the end-to-end vector of each chain, which is defined as

$$\vec{u}_R(t) = \vec{R}(t) / |\vec{R}(t)|$$

and MSAD as

$$MSAD = \delta u_R^2(\tau) = \langle (u_R(t+\tau) - u_R(t))^2 \rangle$$

Using MSAD, one can determine the nanofibers' rotational diffusion, D_r , and the longest relaxation time of the system, $\tau_r \propto D_r^{-1}$.

Next, we assess the mean-squared displacement (MSD) of the nanofibers' centered bead (CB) to learn about the parallel and normal diffusion and ensuing tubing mechanism in a crowded environment as follows⁹

$$\begin{aligned} g_{\parallel}(\tau) &= \langle [(\vec{r}_{CB}(t+\tau) - \vec{r}_{CB}(t)) \cdot \vec{u}_R(t)]^2 \rangle \\ g_{\perp}(\tau) &= \langle [(\vec{r}_{CB}(t+\tau) - \vec{r}_{CB}(t))]^2 \rangle - g_{\parallel}(\tau) \end{aligned}$$

For times shorter than the system's internal relaxation time, contour fluctuation, $\delta R^2(t)$, is the main mechanism, and as a result, $g_{\perp}(t)$ behave similarly to $\delta R^2(t)$ as $t^{3/4}$ ⁸.

S5. A comment on experimental results of Figure 6C

The experimental results (stars) in Figure 6C are taken from Figure 7 and Figure 3 of Nordenström et al.¹⁹. It is essential to note that we have made certain assumptions, such as using the average length given distribution given to calculate ξ_p/L . Moreover, we have considered the Stokes-Einstein assumption for the diffusion coefficient $D = \frac{k_B T}{3\pi\mu a}$.

S6. Tube diameter and entanglement time (τ_e) estimation

Correctness of estimation of tube diameter is so crucial and can affect the other related results like scaling laws that are presented in the study. Here, derivative analysis has been used to identify the crossover point. The rationale behind this method is that the crossover point would manifest as an inflection point, or a significant change in the slope of the MSD-time curve. In mathematical terms, this can be detected by analyzing the first derivative of the curve. Firstly, due to the broad range of the data, it was essential to narrow down to a specific range of time where the crossover was suspected. This prevents potential anomalies or noise from other parts of the curve from misleading the analysis. Secondly, discrete derivative was calculated for the narrowed range.

Given data points (t_i, MSD_i) the derivative at t_i is approximately $\left. \frac{d MSD}{dt} \right|_{t_i} = \frac{MSD_{i+1} - MSD_{i-1}}{t_{i+1} - t_{i-1}}$, except

for the first and last data point. In the next step, the derivative is plotted and analyzed to find the noticeable change. To clarify the procedure, for the case presented in Figure S4, the analysis has been done for $9e - 5 < \tau/\tau_d < 5e - 4$ which is the suspected region. As it can be seen, in Figure S4, the peak in the graph shows the exact entanglement time (τ_e) for this case which is $\tau_e = 0.000121$.

Tables

Table. S1. Simulation parameters

parameter	Value (simulation unit)
Thermal energy (ϵ)	$1[E]$
Nanofiber width (b)	$1[x]$
Time step (τ)	$0.001[t]$
LB time step (τ_f)	$0.001[t]$
Lattice constant (a)	$1[x]$
Kinematic viscosity (ν)	$\nu_w \cdot \frac{\tau_f^2}{a^2}$
Solvent density (ρ)	$k_B T \cdot \frac{\tau_f^2}{a^5 \cdot 1\epsilon}$
σ in WCA potential	$1[x]$
r_{cut} in WCA potential	$1[x] \cdot 2^{1/6}$
r_0 in harmonic potential	$1[x]$
γ friction parameter	$10 \frac{[m]}{[t]}$
Nanofiber length (L)	$50[x] \leq L \leq 300[x]$
Box size (box_l)	$minimum \rightarrow 1.3 L$

Figures

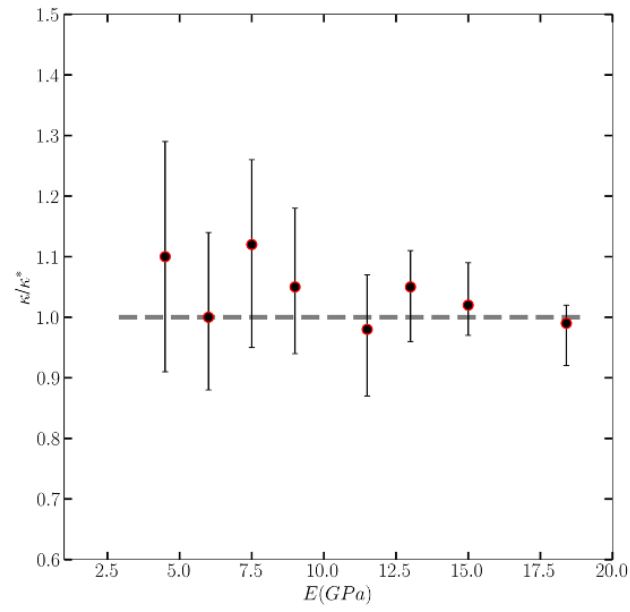


Figure S1. The ratio of bending stiffness from Young's modulus to thermal fluctuation motion κ/κ^* .

When comparing examples of different stiffnesses, it is evident that the error is bigger for less stiff cases owing to the higher rate of thermal motion.

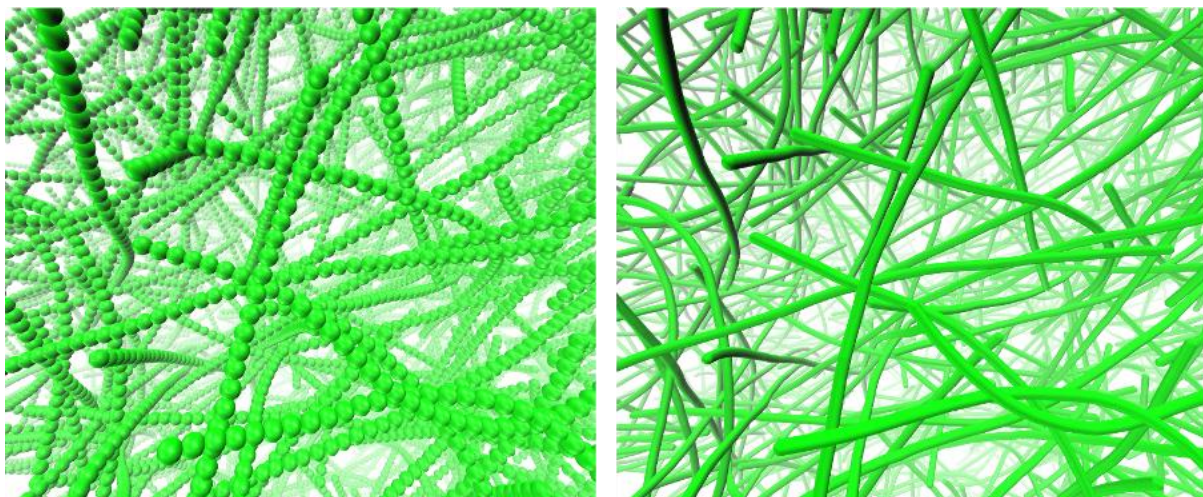


Figure S2. A demonstration of nanofiber modeling for the special situation of $L_p/L=1.5$ and $\xi/L=0.12$. In supplementary Movie S1, the dynamics of nanofiber simulations are also shown.

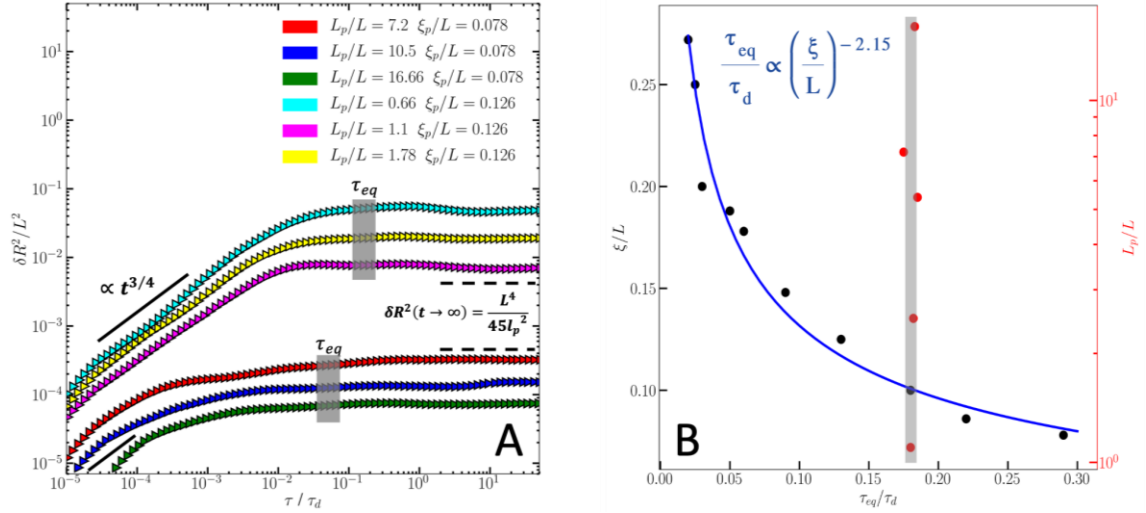


Figure S3. The dependency of τ_{eq} on system crowding (ξ_p/L) and nanofiber stiffness (L_p/L) is shown. A) It is shown that τ_{eq} remains consistent for cases with the same ξ_p/L irrespective of the nanofibers' varying flexibility. The solid line depicts the $t^{3/4}$ trend and it is evident that in dilute scenarios, there is a direct transition from the $t^{3/4}$ behavior to the plateau, without any intermediate phase B) The black circles depict the relationship of τ_{eq} to ξ_p/L , whereas the red circles depict its relationship to L_p/L for special case of $\xi_p/L = 0.11$. Internal relaxation time clearly depends heavily on ξ_p/L as $\left(\tau_{eq}/\tau_d\right) \propto \left(\xi_p/L\right)^{-2.15}$. In a sense, it takes more time for internal relaxations to take place in a crowded environment than in a less crowded one. The internal relaxation time, however, is independent of nanofiber stiffness.

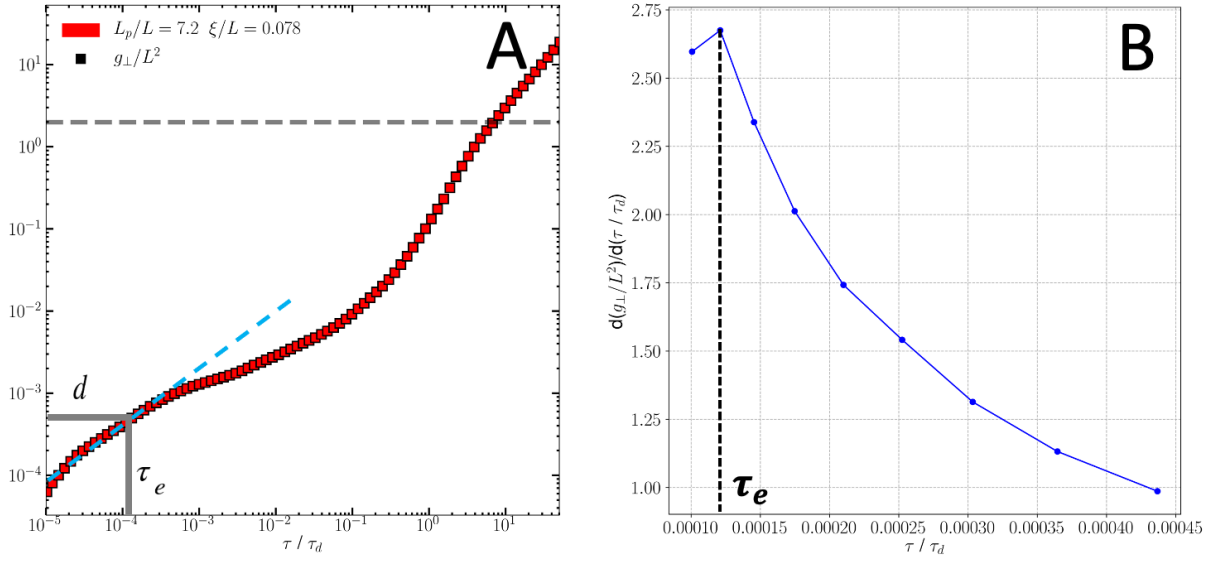


Figure S4. The tube diameter is estimated based on the transition point from $t^{3/4}$ behavior to the entangled regime using discrete derivative analysis. An approximation of the entanglement time, τ_e , may also be obtained using the point's time coordinate. **A)** $g_{\perp}(t)$ plot for the case with $L_p/L=7.2$ and $\xi_p/L=0.078$. $g_{\perp}(t)$ shows the identical behavior of $\delta R^2(t)$ for short times as $t^{3/4}$. **B)** discrete derivative of $g_{\perp}(t)$ versus time. The peak shows the crossover point for tube diameter and τ_e estimations.

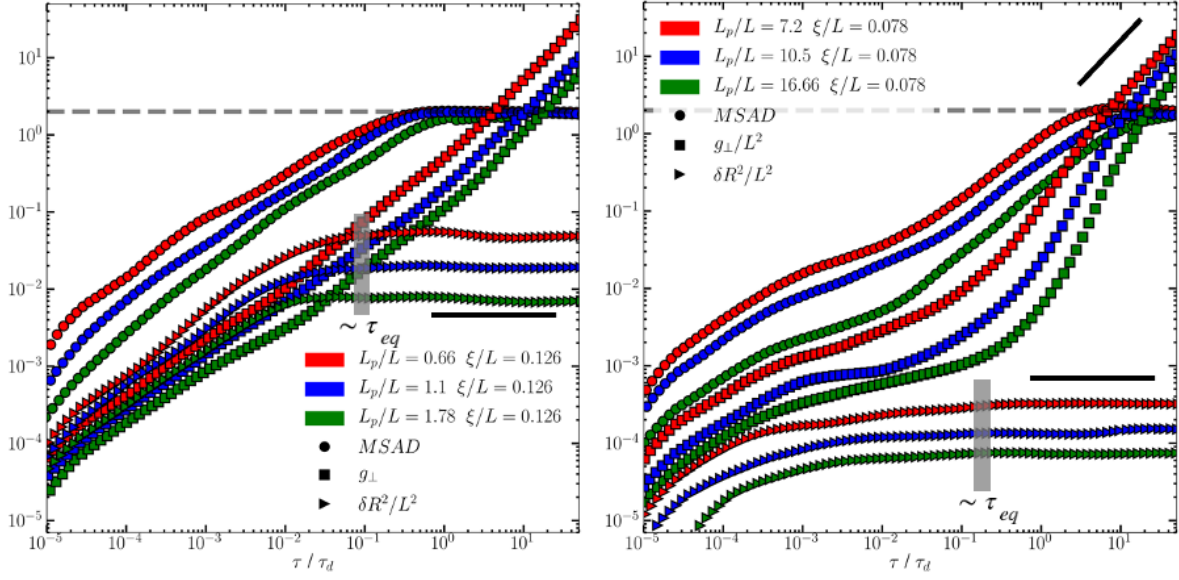


Figure S5. Plotted observables for various cases. As is evident from the $\delta R^2/L^2$ behavior, nanofibers need more time to relax internally in more crowded surroundings (lower ξ_p/L). In addition, based on g_{\perp}/L^2 and $MSAD$, we may conclude that confinement effects are less observable in less crowded environments.

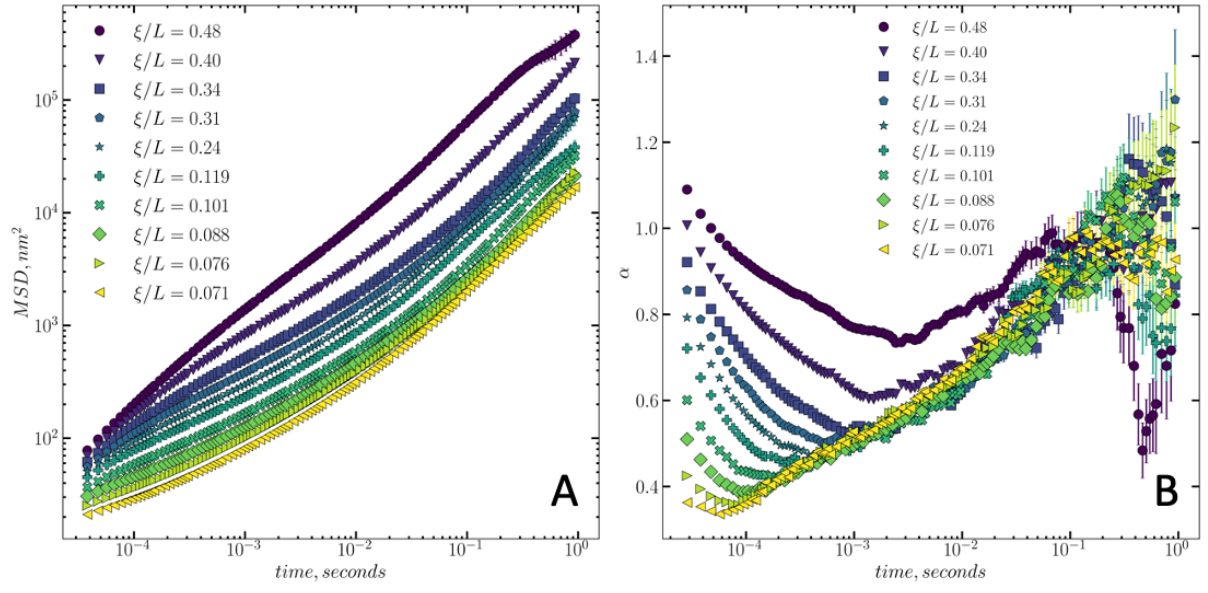


Figure S6. A) Mean-squared displacement of the probe bead as a function of lag time in CNF networks with different mesh sizes, ξ_p/L . The MSD and its error bars are calculated using MUnCH^{2,3}. B) Local exponent in the MSD, α as a function of lag time for the MSDs shown in part A).

Movies

Movie S1. A demonstration of nanofiber modeling for the special situation of $L_p/L = 1.5$ and $\xi/L = 0.12$

Description: 3D rotating view of a simulated polymer network using bead-spring model, highlighting the structure and dynamics of the simulated polymer systems.

Movie S2. Dynamics of a single nanofiber for the case of $L_p/L = 7.2$ and $\xi_p/L = 0.098$: breaking the cage

Description: The movie demonstrates the dynamics of a semi-flexible nanofiber moving in a crowded environment of other dynamic polymers. The nanofiber initially is trapped in a tube but eventually breaks free and continues to rotate and find the next tube. This movie depicts the constraint release mechanism and presence of dynamic cages.

Movie S3. Dynamics of a single fiber: breaking the cage

Description: The movie demonstrates the dynamics of a semi-flexible nanofiber moving in a crowded environment of other dynamic polymers. This movie depicts the constraint release mechanism and presence of dynamic cages for a shorter nanofiber compared to Movie S2.

Movie S4. Dynamics for the case of $L_p/L = 1.9$ and $\xi_p/L = 0.14$ (stiffness effect)

Description: Simulated dynamics of highly flexible nanofibers in a dynamic environment, highlighting early entanglement compared to networks made of nanofibers that are relatively less flexible.

Movie S5. Dynamics for the case of $L_p/L = 3.6$ and $\xi_p/L = 0.14$ (stiffness effect)

Description: Simulated network of nanofibers with lower flexibility, exhibiting lower degree of entanglement compared to a more flexible network.

Movie S6. A test rigid polymer in a fixed static network

Description: The movie presents dynamics of a rigid rod in a static network of other rigid rods. The simulations demonstrate the stability of tubes or cages within the network, providing insight into the behavior of a stiff polymer in a stable tube.

Movie S7. A test rigid polymer in a dynamic system (Kinetic cages)

Description: The movie shows dynamics of a rigid rod in a dynamic network of other moving rods. The dynamics reveal the kinetic nature of the tubes or cages within the network, which have a short lifetime compared to those in a static network.

Movie S8. Empty spaces between the nanofibers with time

Description: The movie aims to provide insight into the creation and dissolution of tubes or cages within a dynamic network of nanofibers. The simulations showcase the empty spaces between the nanofibers and how they contribute to the formation and breakdown of these structures over time.

References

- (1) Ahlrichs, P.; Dünweg, B. Lattice-Boltzmann Simulation of Polymer-Solvent Systems. *Int. J. Mod. Phys. C* **1998**, *9* (08), 1429–1438.
- (2) Córdoba, A.; Schieber, J. D. MUnCH: A Calculator for Propagating Statistical and Other Sources of Error in Passive Microrheology. *Rheol. Acta* **2022**, *61* (1), 49–57.
- (3) Córdoba, A. *Microrheology Uncertainty Calculation Helper (MUnCH)*.
https://github.com/andcorduri/GBD_MUnCH.
- (4) Ethier, J. G.; Nourian, P.; Islam, R.; Khare, R.; Schieber, J. D. Microrheology Analysis in Molecular Dynamics Simulations: Finite Box Size Correction. *J. Rheol. (N. Y. N. Y.)* **2021**, *65* (6), 1255–1267.
- (5) Mason, T. G. Estimating the Viscoelastic Moduli of Complex Fluids Using the Generalized Stokes–Einstein Equation. *Rheol. acta* **2000**, *39* (4), 371–378.
- (6) Jones, C. W.; Wang, J. C.; Ferrone, F. A.; Briehl, R. W.; Turner, M. S. Interactions between Sick Hemoglobin Fibers. *Faraday Discuss.* **2003**, *123*, 221–235.
- (7) Usov, I.; Nyström, G.; Adamcik, J.; Handschin, S.; Schütz, C.; Fall, A.; Bergström, L.; Mezzenga, R. Understanding Nanocellulose Chirality and Structure–Properties Relationship at the Single Fibril Level. *Nat. Commun.* **2015**, *6* (1), 1–11.
- (8) Granek, R. From Semi-Flexible Polymers to Membranes: Anomalous Diffusion and Reptation. *J. Phys. II* **1997**, *7* (12), 1761–1788.
- (9) Nam, G.; Johner, A.; Lee, N.-K. Reptation of a Semiflexible Polymer through Porous Media. *J. Chem. Phys.* **2010**, *133* (4), 44908.
- (10) De Gennes, P.-G. Reptation of a Polymer Chain in the Presence of Fixed Obstacles. *J. Chem. Phys.* **1971**, *55* (2), 572–579.
- (11) Doi, M.; Edwards, S. F. Dynamics of Concentrated Polymer Systems. Part 1.—Brownian

- Motion in the Equilibrium State. *J. Chem. Soc. Faraday Trans. 2 Mol. Chem. Phys.* **1978**, 74, 1789–1801.
- (12) Doi, M. Explanation for the 3.4- power Law for Viscosity of Polymeric Liquids on the Basis of the Tube Model. *J. Polym. Sci. Polym. Phys. Ed.* **1983**, 21 (5), 667–684.
- (13) Graessley, W. W. Entangled Linear, Branched and Network Polymer Systems—Molecular Theories. In *Synthesis and Degradation Rheology and Extrusion*; Springer, 1982; pp 67–117.
- (14) Doi, M.; Graessley, W. W.; Helfand, E.; Pearson, D. S. Dynamics of Polymers in Polydisperse Melts. *Macromolecules* **1987**, 20 (8), 1900–1906.
- (15) Marrucci, G. Relaxation by Reptation and Tube Enlargement: A Model for Polydisperse Polymers. *J. Polym. Sci. Polym. Phys. Ed.* **1985**, 23 (1), 159–177.
- (16) Perkins, T. T.; Smith, D. E.; Chu, S. Direct Observation of Tube-like Motion of a Single Polymer Chain. *Science* (80-.). **1994**, 264 (5160), 819–822.
- (17) Read, D. J.; Jagannathan, K.; Likhtman, A. E. Entangled Polymers: Constraint Release, Mean Paths, and Tube Bending Energy. *Macromolecules* **2008**, 41 (18), 6843–6853.
- (18) Rubinstein, M.; Colby, R. H. Self- consistent Theory of Polydisperse Entangled Polymers: Linear Viscoelasticity of Binary Blends. *J. Chem. Phys.* **1988**, 89 (8), 5291–5306.
- (19) Nordenström, M.; Benselfelt, T.; Hollertz, R.; Wennmalm, S.; Larsson, P. A.; Mehandezhiyski, A.; Rolland, N.; Zozoulenko, I.; Söderberg, D.; Wågberg, L. The Structure of Cellulose Nanofibril Networks at Low Concentrations and Their Stabilizing Action on Colloidal Particles. *Carbohydr. Polym.* **2022**, 297, 120046.